Supporting Information: Screening Links Transport and Recombination Mechanisms in Lead Halide Perovskites

Casey L. Kennedy[1], Andrew H. Hill[2], Erik M. Grumstrup[*,1,2].
[1]Department of Chemistry, Montana State University, Bozeman, MT 59717, U.S.
[2]Montana Materials Science Program, Montana State University, Bozeman, MT 59717, U.S.

Experimental

Material Synthesis and Thin-Film Fabrication: Precursor solutions for $CsPbBr_3$ thin-films were prepared by dissolving a 1:1 molar ratio of $PbBr_2$ and CsBr in DMSO at 65 °C. Due to insolubility of CsBr, $PbBr_2$ was dissolved first and then CsBr was added. Precursor solutions for $MAPbBr_3$ thin-films were prepared by dissolving a 1:1 molar ratio of $PbBr_2$ and dehydrated MABr in DMF at 65 °C. Once precursors solutions were prepared, 200 µL of either $CsPbBr_3$ or $MAPbBr_3$ solution was spin-casted onto a glass substrate for 20s at 750 rpm. Immediately after spin-casting, $CsPbBr_3$ samples were annealed at 85 °C in a saturated DMSO atmosphere and $MAPbBr_3$ samples were annealed at 80 °C in a saturated DMF atmosphere, each for one hour. After the annealing process, thin film samples were covered with a microscope slide and sealed using clear enamel. $MAPbI_3$ samples were prepared as previously described.[1]

Ultrafast Microscopy: Pump-probe experiments were carried out using a home-built ultrafast pump-probe microscope. The primary excitation source is a Ti: sapphire oscillator which emits 70 fs pulses at 80 MHz and is tunable between 690 and 1040nm. The fundamental (850nm for $CsPbBr_3$ and 800nm for $MAPbBr_3$) is split into two separate lines, the pump and probe. The probe is aligned onto a translation stage, then coupled onto a set of galvanometer mirrors. The translation stage is used to temporally separate the pump and probe pulses and galvanometer mirrors are used to scan the probe and pump beams independently of one another. The pump is frequency doubled via a BBO crystal then recombined with the probe using a dichroic beam splitter. Both the pump and probe are sent through a 4f lens system before being coupled into a second set of galvanometer mirrors and passed through a second 4f lens system. The two coupled 4f-galvanometer pairs provide the ability to independently position pump and probe. Finally, the pump and probe are focused onto the sample using a 100x (0.90NA) microscope objective. The reflected probe signal is detected using a balanced photodiode coupled to a lock-in amplifier.

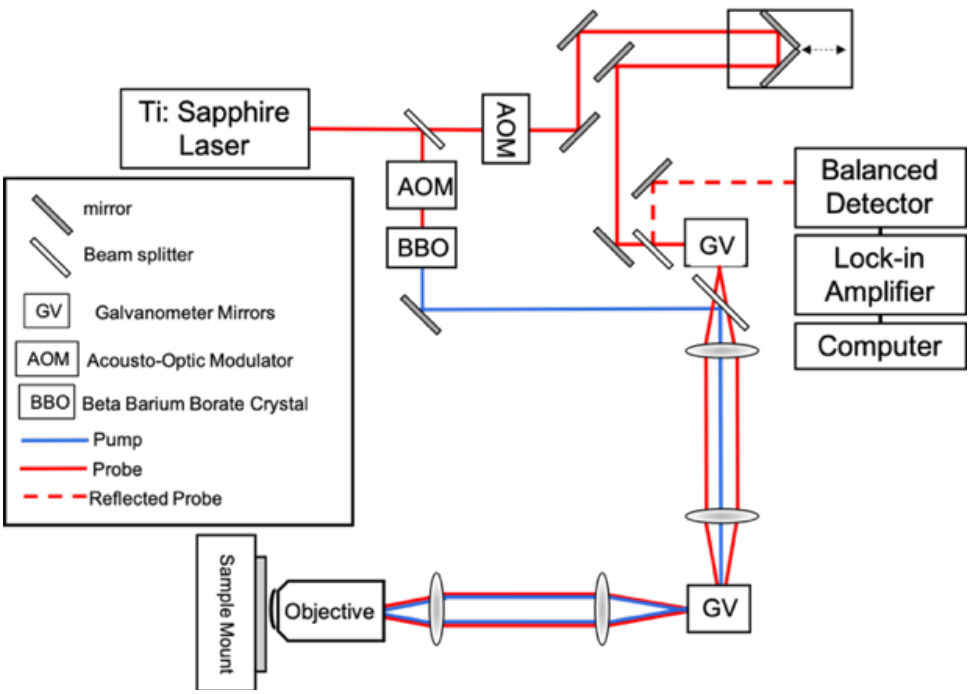

Figure S1. Diagram of home-build femtosecond microscope.

Data Analysis

Gaussian Pump Spot Size and Carrier Density: The focused pump-pulse is modeled as a two-dimensional Gaussian:

$$g[r] = \frac{I_0 \, \mathrm{Log}[2]}{\beta^2 \, \pi} \mathrm{Exp}\left[\frac{-4 \, \mathrm{Log}[2] \, r^2}{\beta^2}\right] \qquad \text{(S1)}$$

I_0 is the measured energy of the pump pulse, accounting for transmittance of the pump light through the microscope objective and reflection off the cover slip and sample. β is the full-width at half-maximum of the focused beam on the sample. To determine β, a SiC nanowire of sub-diffraction width (~140nm) is imaged by the pump beam and fit by a model which convolves a hemispherical profile (defined to be the same width of the nanowire, as determined by scanning electron microscopy) with a gaussian pump pulse. Modeling performed on three different SiC nanowires produced an average pump FWHM of $\beta \approx 300\mathrm{nm}$. Fluence is calculated using Eq. S2, where r_0 is the $1/e^2$ width of the pulse.

$$G[r] = \frac{\int_0^{2\pi} \int_0^{r_0} g[r] \, r \, \partial r \, \partial\theta}{\int_0^{2\pi} \int_0^{r_0} r \, \partial r \, \partial\theta} \qquad \text{(S2)}$$

Carrier densities are calculated using Eq. S3, where α is the extinction coefficient of the material.

$$N = \frac{\int_0^{2\pi} \int_0^{r_0} \int_0^{1/\alpha} G[r] \, \alpha \, \mathrm{Exp}[-\alpha \, z] \, r \, \partial z \, \partial r \, \partial\theta}{\int_0^{2\pi} \int_0^{r_0} \int_0^{1/\alpha} r \, \partial z \, \partial r \, \partial\theta} \qquad \text{(S3)}$$

Carrier Diffusion: Carrier diffusion was measured by directly imaging the spatial evolution of the excited state. For these spatially separated measurements, the probe is scanned over the excited pump volume at a series of increasing pump-probe delay times. Each image is integrated along one axis and the resulting profiles are fit to gaussians. The squares of the time-dependent FWHMs are plotted vs. time. The slope of the fit is proportional to the diffusion constant via:

$$\Delta\beta^2 = \beta(t_0)^2 + 16\ln(2)\, D_{am} \cdot (\Delta t - t_0) \qquad \text{(S4)}$$

$\beta(t_0)^2$ is the square of the normalized excited-state distribution profile FWHM when $\Delta t = 0$ and D_{am} is the ambipolar diffusion constant.

Carrier Density Dependence of ΔR: Panels (A) and (C) of Figure S2 show representative TR decay kinetics taken from individual $CsPbBr_3$ and $MAPbBr_3$ perovskite domains, respectively. Panels (B) and (D) illustrate the linear dependence of $-\Delta R_{t=0}$ on carrier density over the entire range measured ($1.48\times 10^{18} - 1.19 \times 10^{19}\text{cm}^{-3}$).

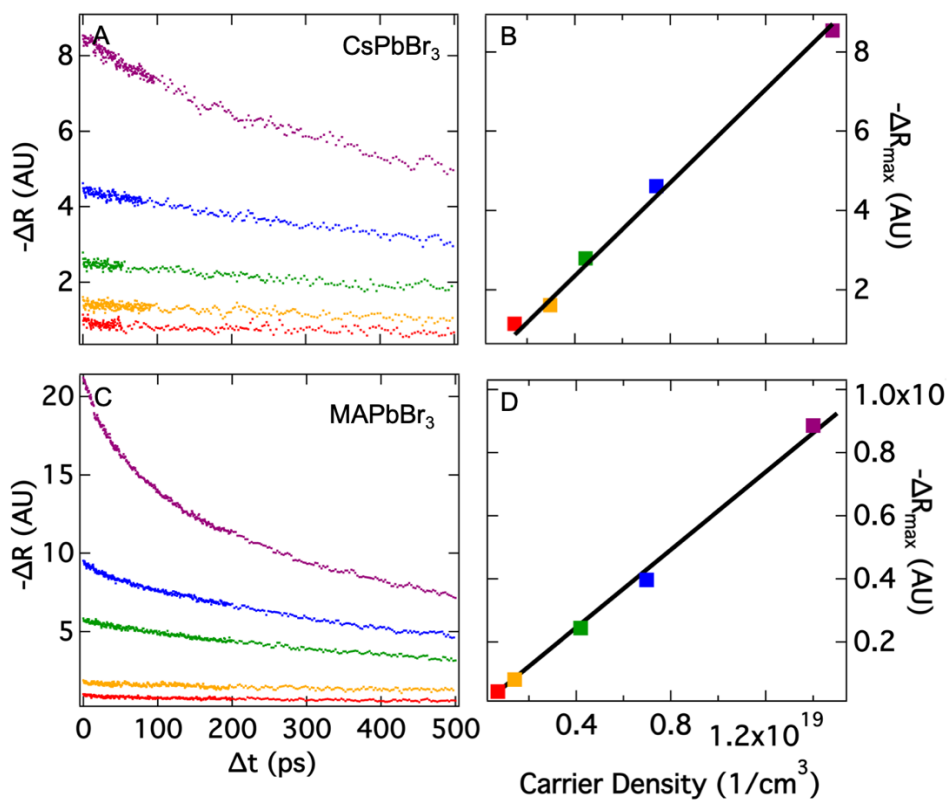

Figure S2 Excitation-Fluence Dependent TR Decay Kinetics. Red, yellow, green, blue and purple dots correspond to kinetics data taken on $CsPbBr_3$ (A) and $MAPbBr_3$ (C) at increasing carrier densities scaled to the lowest carrier density measured ($1.48\times 10^{18}\text{cm}^{-3}$ for $CsPbBr_3$ and $6.98\times 10^{17}\text{cm}^{-3}$ for $MAPbBr_3$. Panels (B) and (D) shows that $-\Delta R$ at $\Delta t = 0$ ps scales linearly with carrier density up to $1.48\times 10^{19}\text{cm}^{-3}$ and $1.40 \times 10^{19}\text{cm}^{-3}$ for $CsPbBr_3$ and $MAPbBr_3$, respectively. Note the y-intercepts on each of the fits is equal to 0.

Nonlinear Carrier Recombination: Figure S3 shows a series of excitation dependent kinetics taken on an individual $CsPbBr_3$ domain. Low fluence recombination occurs primarily via first-order (trap-mediated) processes, as shown by the black dots in Fig. S3A. To best visualize contributions from higher-order processes to the observed recombination dynamics, we have removed contributions from first-order processes. Figure S3B shows the kinetics in (A) with the time dependent amplitude of the lowest fluence trace (black dots) subtracted from each kinetics trace in the series. To quantitate the fraction of carriers recombination occurring via second and third order processes, ($\Delta\Delta R_{NORM}$), the magnitude of each trace in Fig. S3B at $\Delta t = 600$ps was normalized to the initial decay of the lowest fluence trace and then plotted vs. carrier density (Fig. 3D).

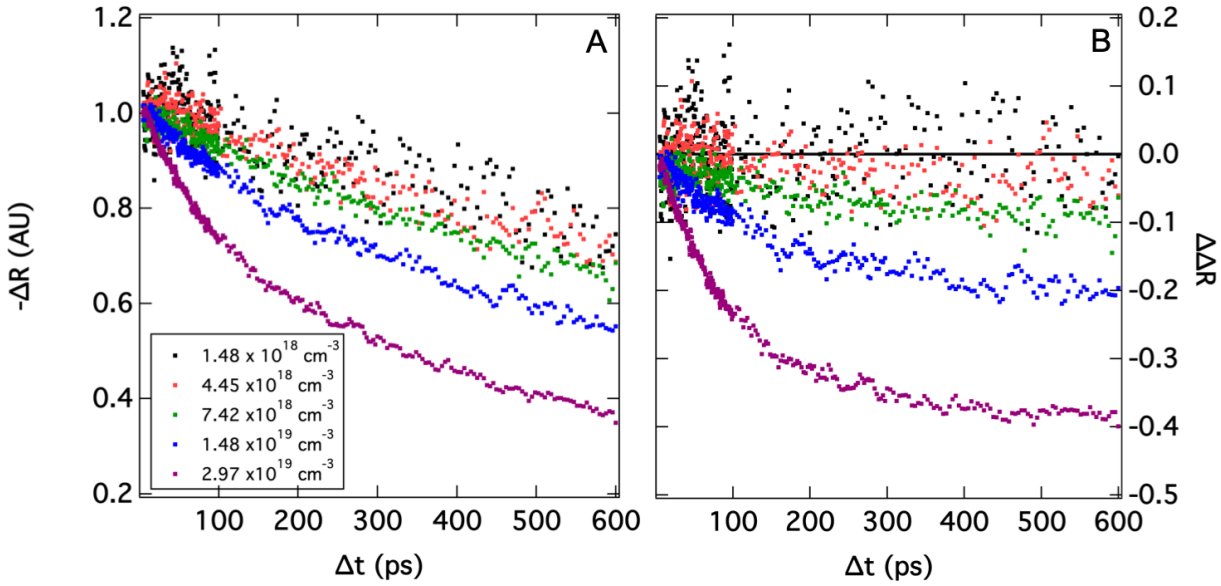

Figure S3 Higher-order Carrier Recombination: Panel (A) shows a series of excitation-fluence dependent kinetics measurements taken on a single crystalline $CsPbBr_3$ perovskites. Panel (B) shows the kinetics measurements in (A) after removing contributions from first-order recombination.

Figure S4 compares $\Delta\Delta R_{norm}$ values determined from modeled recombination kinetics, where k_1 is increased from $k_1 = 0.0007$ ps^{-1} (Fig S4A) to $k_1 = 0.0012$ ps^{-1} (Fig S4B). These values of k_1 give rise to kinetics that closely approximate the difference in low-density recombination kinetics in Figure 3A and 3C. For a given set of nonlinear recombination coefficients, $k_2 = 2.0 \times 10^{-10}$ μm^3/ps, and $k_3 = 1.0 \times 10^{-18}$ μm^6/ps, the difference in the $\Delta\Delta R_{norm}$ determined from the kinetics (Fig S4C) lies within the experimental uncertainty.

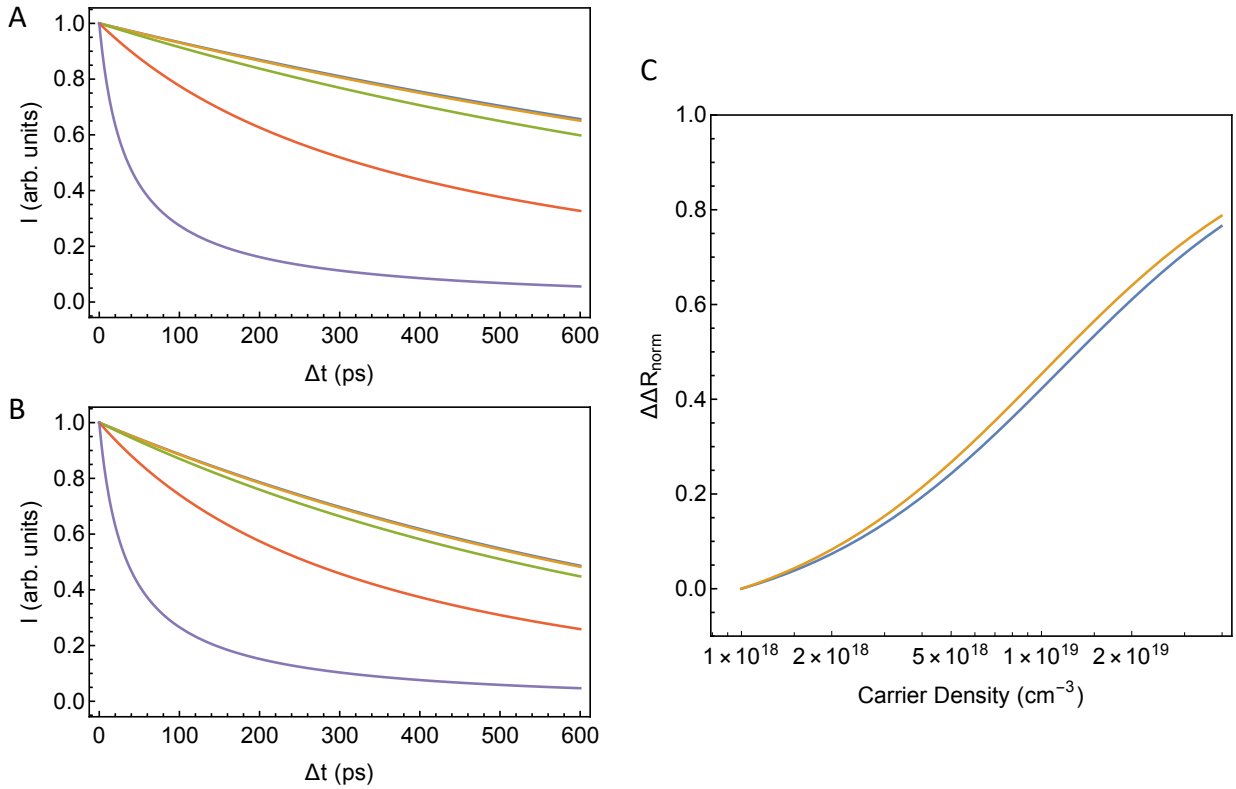

Figure S4 Effects of faster first order recombination on ΔΔR determination. Panel A shows modeled recombination kinetics (between 1×10^{18} and 4×10^{19} cm^{-3}) assuming a first order rate constant of $k_1 = 0.0007$ ps^{-1}, a second order term, $k_2 = 2.0 \times 10^{-10}$ $\mu m^3/ps$, and a third order term, $k_3 = 1.0 \times 10^{-18}$ $\mu m^6/ps$. Panel B shows modeled decay kinetics with the nonlinear recombination terms held constant and with $k_1 = 0.0012$ ps^{-1}. Panel C shows a comparison of ΔΔR determined at Δt = 600 ps for the kinetics shown in panels A (yellow) and B (blue).

Estimation of error in measured D_{am} introduced by nonlinear recombination: In a continuum approximation of the photoexcited carrier density, the temporal and spatial evolution is given (in one dimension) by,

$$\frac{\partial n(t)}{\partial t} = D_{am}\frac{\partial^2 n(t)}{\partial x^2} - k_1 n(t) - k_2 n(t)^2 - k_3 n(t)^3. \qquad \text{(S5)}$$

The first term describes the diffusive motion of charges, and k_1, k_2, and k_3 describe trap-mediated, radiative (bimolecular), and Auger recombination, respectively. Because the center of the excitation profile has higher carrier density, nonlinear recombination can cause the gaussian carrier profile to "flatten out," which can be interpreted as an apparently faster diffusive process than the nominal D_{am}. To estimate the magnitude of this effect, we numerically solved Eq. S5 at a series of excitation densities (calculated as described above), convolved the carrier profile with a gaussian to model the spatial scanning of the probe beam in our instrument, and fit the resultant profiles to extract the diffusion coefficient (also as described above for experimental measurements). Figure S5 shows the results of this modeling. Panel A shows power-dependent recombination kinetics. At high densities, the nonlinear recombination terms enhance recombination leading to faster decay. Panels B and C show profiles from low and high initial carrier densities. Panel D shows the fit-determined diffusion constants determined by fitting these profiles. In the case of higher

excitation density, the nonlinear recombination causes an apparent 13% increase in the measured diffusion coefficient.

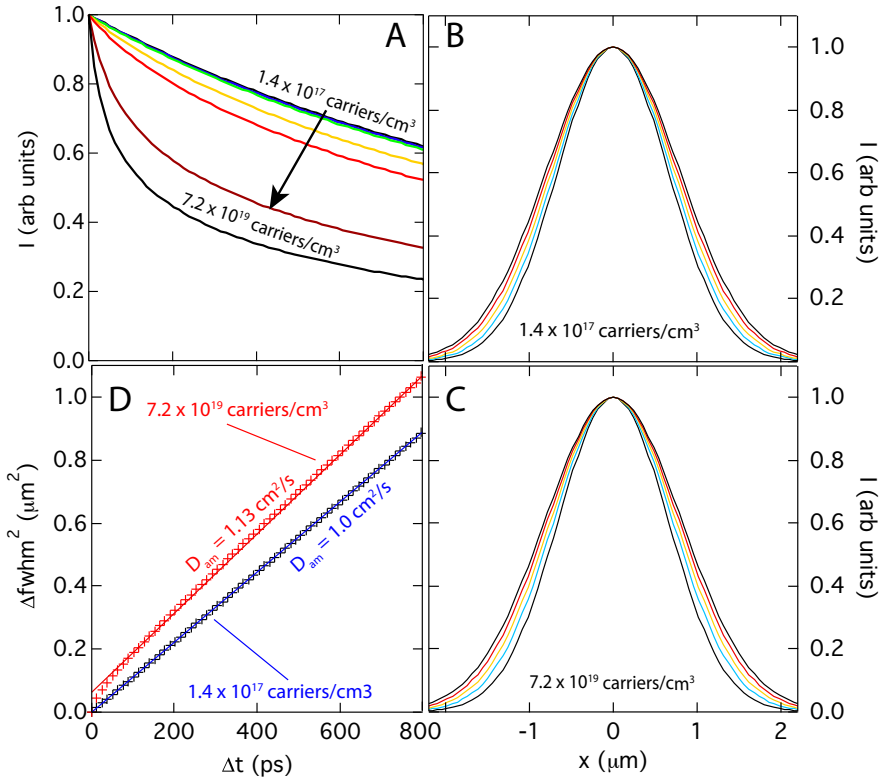

Figure S5 Estimation of error associated with nonlinear recombination. Panel A shows modeled kinetics for increasing excitation densities from 1.4×10^{17} cm^{-3} to 7.2×10^{19} cm^{-3}, assuming $D_{am} = 1.0$ cm^2/s, $k_1 = 2 \times 10^{-4}$ ps^{-1}, $k_2 = 1 \times 10^{-10}$ cm^3 s^{-1}, and $k_3 = 1 \times 10^{-29}$ cm^6 s^{-1} and a 300 nm fwhm gaussian pump pulse. Panels B and C show the time dependent profiles (at Δt = 0, 250, 500, 750, and 1000 ps), obtained by convolving the probe with the evolving carrier density. Panel D shows the difference in apparent diffusion coefficients, obtained by finding the slope of a best-fit line to the $fwhm^2(\Delta t)$ obtained from profiles like those shown in panels B and C. The apparent 13% increase in D_{am} at high excitation densities is a result of nonlinear recombination, which decreases the signal amplitude near the middle of the profiles (panels B and C) where carrier density is highest.

Optical Dielectric: Given a probe energy far below the optical bandgap of the material, the optical dielectric is given by the square of the real index of refraction ($\epsilon_\infty = n^2$). To determine n, both a ground state reflective image (GSR) and an atomic force micrograph (AFM) of a single domain are collected. The two images (GSR and AFM) are pixel matched and interpolated so that correlated data points from each image lay at the same grid position. A median filter is applied to the GSR image to eliminate any low frequency background and center the fringes at R = 0. The filtered ground state images are fit with a Gaussian broadened transfer matrix model to account for the limited spatial resolution of the microscope. A detailed description of the transfer matrix fitting protocol can be found in a previous publication.[2] A representative example of the transfer matrix fitting protocol (TMF) applied to a $CsPbBr_3$ domain is shown in Figure S6.

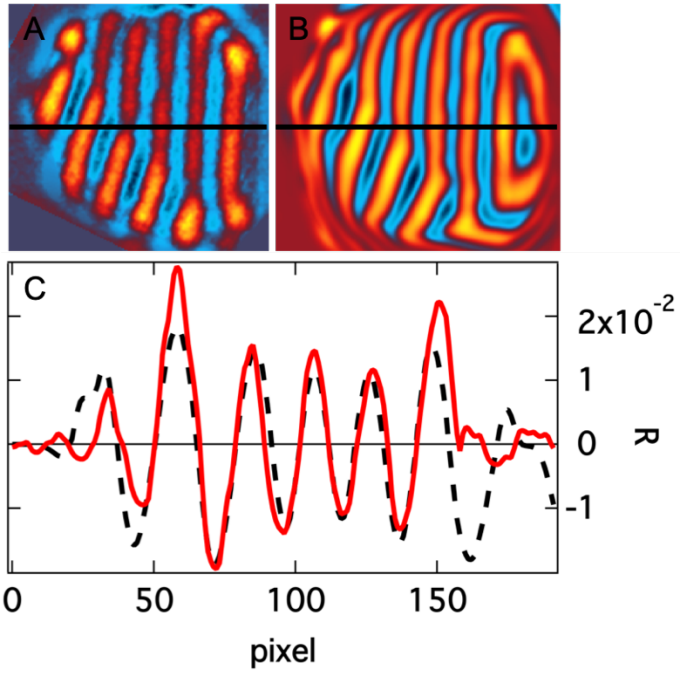

Figure S6 Determination of n in an individual $CsPbBr_3$ domain. (A) Experimental and (B) modeled ground state reflective image of a single crystalline $CsPbBr_3$ domain assuming a refractive index of n = 2.3. (C) Slices of the GSR image (red) and modeled image (black) taken from the black lines in figures (A) and (B), respectively. Note deviations from the model near the edge of the domain are primarily due to surface roughness.

Steady State Spectra: Scanning electron micrographs (SEMs) representative of single crystalline domains on $MAPbBr_3$ (Fig. S7A) and $CsPbBr_3$ (Fig. S7B) thin-films are shown below. The corresponding absorption and emission spectra determine a bandgap energy of 2.30eV for $MAPbBr_3$ and 2.37eV for $CsPbBr_3$.

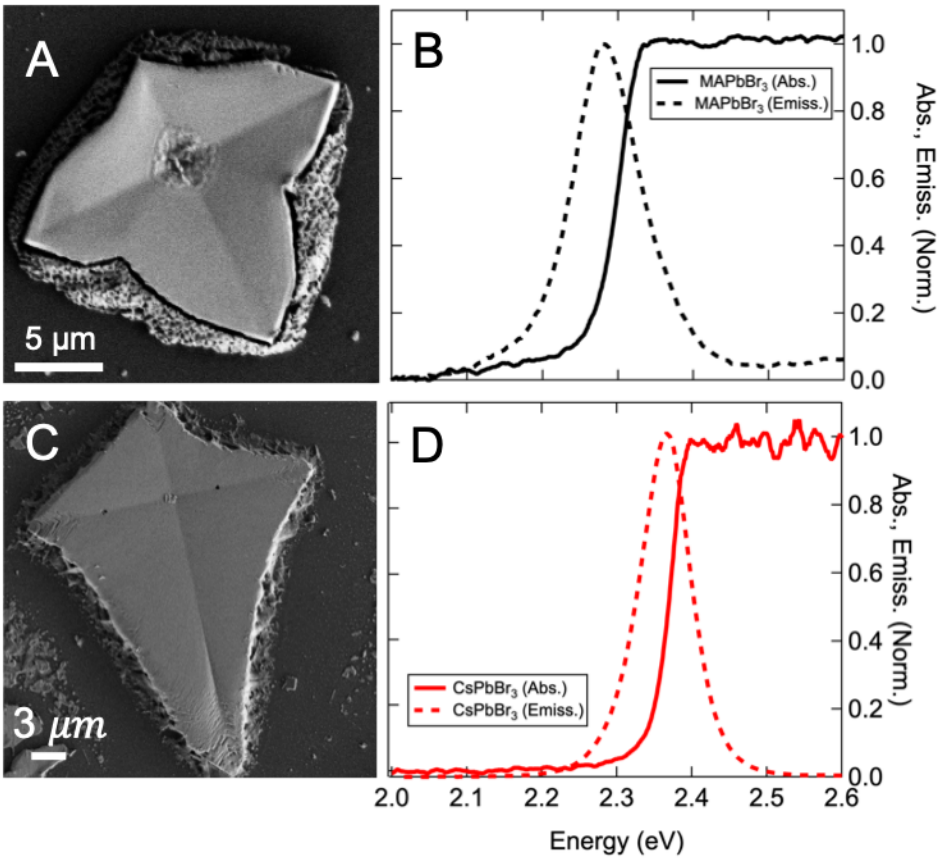

Figure S7 Steady state spectra of $MAPbBr_3$ and CsPbBr. (A) and (C) show representative SEMs of single crystalline $MAPbBr_3$ and $CsPbBr_3$ domains, respectively. (B) and (D) show emission and absorption spectra taken on $MAPbBr_3$ and $CsPbBr_3$ thin-film. The bandgaps for $MAPbBr_3$ and $CsPbBr_3$ are 2.30eV and 2.37eV, respectively.

Reported Reduced Masses: The following table lists reduced masses reported in literature for the three perovskite species study in this manuscript.

Perovskite	μ
$CsPbBr_3$	0.126[3], 0.073[4], 0.115[5]
$MAPbBr_3$	0.144[6], 0.117[7]
$MAPbI_3$	0.135[6], 0.128[8], 0.104[7]

Table S1 Reported Reduced Masses. The range of reduced masses reported in the literature for $CsPbBr_3$, $MAPbBr_3$ and $MAPbI_3$ is 0.104 to 0.144.

References

1. Hill, A. H.; Smyser, K. E.; Kennedy, C. L.; Massaro, E. S.; Grumstrup, E. M. Screened Charge Carrier Transport in Methylammonium Lead Iodide Perovskite Thin Films. J. Phys. Chem. Lett. **2017,** 8 (5), 948-953.
2. Hill, A. H.; Kennedy, C. L.; Massaro, E. S.; Grumstrup, E. M. Perovskite Carrier Transport: Disentangling the Impacts of Effective Mass and Scattering Time Through Microscopic Optical Detection. J. Phys. Chem. Lett. **2018,** 9 (11), 2808-2813.
3. Yang, Z.; Surrente, A.; Galkowski, K.; Miyata, A.; Portugall, O.; Sutton, R. J.; Haghighirad, A. A.; Snaith, H. J.; Maude, D. K.; Plochocka, P.; Nicholas, R. J. Impact of the Halide Cage on the Electronic Properties of Fully Inorganic Cesium Lead Halide Perovskites. ACS Energy Lett. **2017,** 2 (7), 1621-1627.
4. Kang, Y.; Han, S. Intrinsic Carrier Mobility of Cesium Lead Halide Perovskites. Physical Review Applied **2018,** 10 (4), 044013.
5. Yettapu, G. R.; Talukdar, D.; Sarkar, S.; Swarnkar, A.; Nag, A.; Ghosh, P.; Mandal, P. Terahertz Conductivity within Colloidal CsPbBr3 Perovskite Nanocrystals: Remarkably High Carrier Mobilities and Large Diffusion Lengths. Nano Lett. **2016,** 16 (8), 4838-4848.
6. Mosconi, E.; Umari, P.; De Angelis, F. Electronic and Optical Properties of MAPbX3 Perovskites (X = I, Br, Cl): A Unified DFT and GW Theoretical Analysis. Phys. Chem. **2016,** 18 (39), 27158-27164.
7. Galkowski, K.; Mitioglu, A.; Miyata, A.; Plochocka, P.; Portugall, O.; Eperon, G. E.; Wang, J. T.-W.; Stergiopoulos, T.; Stranks, S. D.; Snaith, H. J.; Nicholas, R. J. Determination of the Exciton Binding Energy and Effective Masses for Methylammonium and Formamidinium Lead Tri-Halide Perovskite Semiconductors. Energy & Environmental Science **2016,** 9 (3), 962-970.
8. Giorgi, G.; Fujisawa, J.; Segawa, H.; Yamashita, K. Small Photocarrier Effective Masses Featuring Ambipolar Transport in Methylammonium Lead Iodide Perovskite: A Density Functional Analysis. J. Phys. Chem. Lett. **2013,** 4 (24), 4213-4216.